iScience

CellPress
OPEN ACCESS

Article

Li/Na substitution and Yb^{3+} co-doping enabling tunable near-infrared emission in $LiIn_2SbO_6:Cr^{3+}$ phosphors for light-emitting diodes

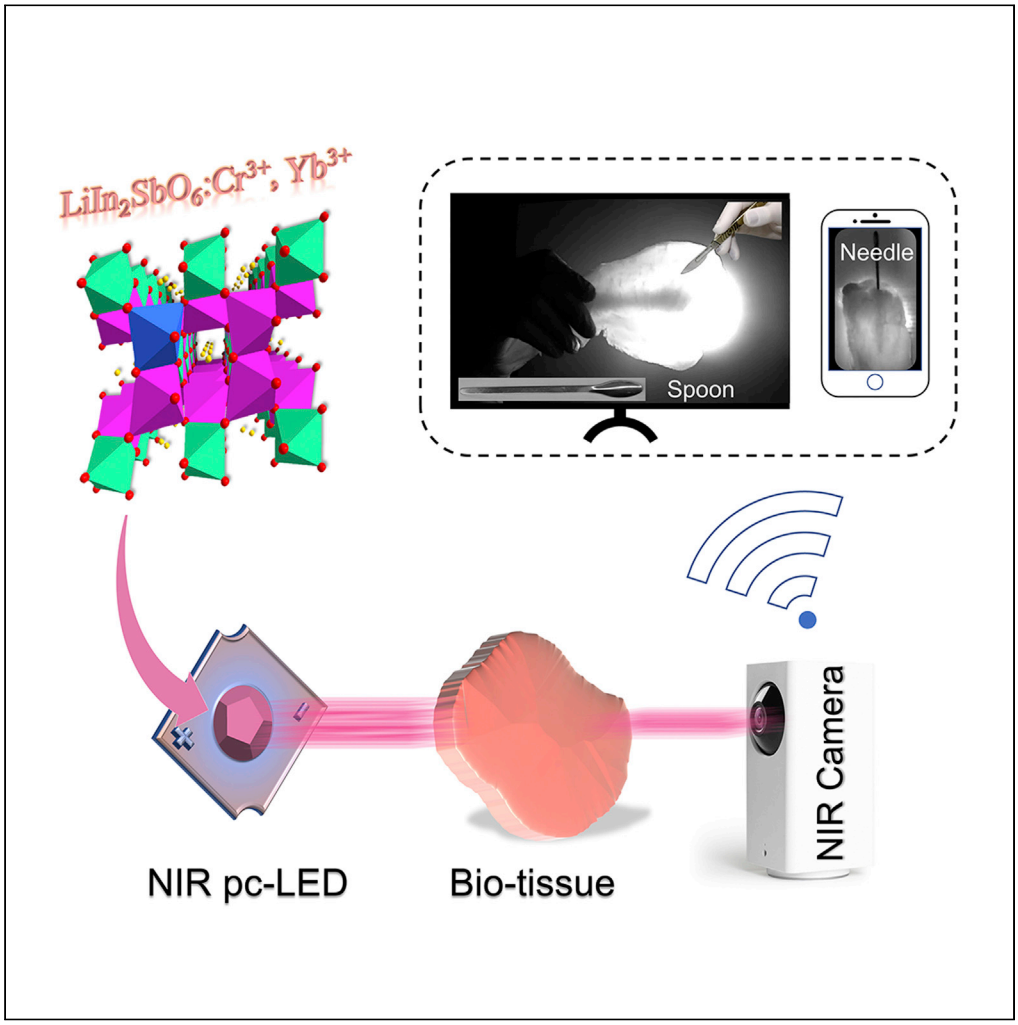

Gaochao Liu, Tao Hu, Maxim S. Molokeev, Zhiguo Xia

xiazg@scut.edu.cn

HIGHLIGHTS

$LiIn_2SbO_6:Cr^{3+}$ exhibits near-infrared emission in the range 780-1400 nm

Li^+/Na^+ substitution in $LiIn_2SbO_6:Cr^{3+}$ enables peak shift from 970 nm to 1020 nm

Efficient energy transfer process from Cr^{3+} to Yb^{3+} is reported

The application of $LiIn_2SbO_6:Cr^{3+},Yb^{3+}$ phosphor in non-invasive detection is demonstrated

Liu et al., iScience 24, 102250
April 23, 2021 © 2021 The Author(s).
https://doi.org/10.1016/j.isci.2021.102250

iScience

CellPress
OPEN ACCESS

Article

Li/Na substitution and Yb^{3+} co-doping enabling tunable near-infrared emission in $LiIn_2SbO_6:Cr^{3+}$ phosphors for light-emitting diodes

Gaochao Liu,[1] Tao Hu,[1] Maxim S. Molokeev,[2,3,4] and Zhiguo Xia[1,5,*]

SUMMARY

Near-infrared (NIR) phosphor-converted light-emitting diode (pc-LED) has great potential in non-invasive detection, while the discovery of tunable broadband NIR phosphor still remains a challenge. Here, we report that Cr^{3+}-activated $LiIn_2SbO_6$ exhibits a broad emission band ranging from 780 to 1400 nm with a full width at half maximum (FWHM) of 225 nm upon 492 nm excitation. The emission peaks are tuned from 970 to 1020 nm together with considerable broadening of FWHM (~285 nm) via Li/Na substitution. Depending on Yb^{3+} co-doping, a stronger NIR fluorescence peak of Yb^{3+} appears with improved thermal resistance, which is ascribed to efficient energy transfer from Cr^{3+} to Yb^{3+}. An NIR pc-LED package has been finally designed and demonstrated a remarkable ability to penetrate pork tissues (~2 cm) so that the insertion depth of a needle can be observed, indicating that the phosphor can be applied in non-destructive monitoring.

INTRODUCTION

Near-infrared (NIR) luminescence materials have been extensively investigated over the past decades for their flexible applications, ranging from night vision, remote control, security system, and other traditional directions to emerging areas such as bioimaging, food component identification, iris recognition, optical communication, targeted therapy, and tumor tissue diagnosis (Wang et al., 2019; Zhang et al., 2019; Qiao et al., 2019; Chan et al., 2020). In particular, the popularization and multifunctional trend of smart devices have stimulated researchers to design a lightweight broadband NIR light source that can be integrated with a real-time analysis component. Although traditional halogen tungsten lamps show an ultra-broadband emission cover from near-violet to middle-infrared region, they are suspended by large sizes, poor efficiency, short life span, high spherical temperature, and long response time (Rajendran et al., 2018). NIR light-emitting diodes (LEDs) also fail to meet the requirements of spectroscopy analysis technology due to their narrow full width at half maximum (FWHM) (Liu et al., 2020a, 2020b; Małysa, 2019). Therefore, numerous investigations on exploring new broadband NIR luminescent materials have been done, which involves quantum dots, fluorescent glasses, phosphors, polymer nanocrystals, organic metal halides, organic LEDs, and so forth (Huang et al., 2020; Cao et al., 2019; Fang et al., 2020; Tessler et al., 2002; Tan et al., 2014; Gong et al., 2016). Recently, NIR phosphor-converted LEDs (pc-LEDs) have become the subject of focused interests owing to their tunable broadband emission, high radiant power, good durability, and simple preparation method by coating the NIR phosphor on a commercial InGaN blue chip.

Since the optical performance of NIR pc-LEDs mainly depends on the phosphors used, intensive efforts have been made to exploit broadband NIR phosphors *via* rare-earth ion- (Eu^{2+}), transition metal ion- (Cr^{3+}, Ni^{2+}, Mn^{2+}, Fe^{3+}), or Bi ion (Bi^{+}, Bi^{3+})-activated inorganic matrices (Tang et al., 2020; Gao et al., 2020; Song et al., 2019; Wei et al., 2020; Guan et al., 2020). Unfortunately, single invisible fluorescence emissions of Eu^{2+}, Mn^{2+}, and Fe^{3+} ions are hard to acquire, and their emissions FWHM are insufficient (Berezovskaya et al., 2013; Song et al., 2015; Zhou et al., 2020). Although Ni^{2+} and Bi ion-activated crystal or glass materials usually exhibit an ultra-broadband emission in the second NIR window (NIR-II, 1000-1700 nm), their luminous efficiency is disappointed (Cao et al., 2018; Xiong et al., 2020). On the contrary, Cr^{3+} ion has been considered as an ideal NIR luminescence center in view of its high quantum efficiency and tunable emission spectrum in 650-1600 nm which strongly depends on the crystal field strength (Bai et al., 2018). For

[1]State Key Laboratory of Luminescent Materials and Devices, Guangdong Provincial Key Laboratory of Fiber Laser Materials and Applied Techniques, Guangdong Engineering Technology Research and Development Center of Special Optical Fiber Materials and Devices, School of Materials Science and Engineering, South China University of Technology, Guangzhou 510641, China

[2]Laboratory of Crystal Physics, Kirensky Institute of Physics, Federal Research Center KSC SB RAS, Krasnoyarsk 660036, Russia

[3]Siberian Federal University, Krasnoyarsk 660041, Russia

[4]Research and Development Department, Kemerovo State University, Kemerovo 650000, Russia

[5]Lead contact

*Correspondence: xiazg@scut.edu.cn

https://doi.org/10.1016/j.isci.2021.102250

This is an open access article under the CC BY-NC-ND license (http://creativecommons.org/licenses/by-nc-nd/4.0/).

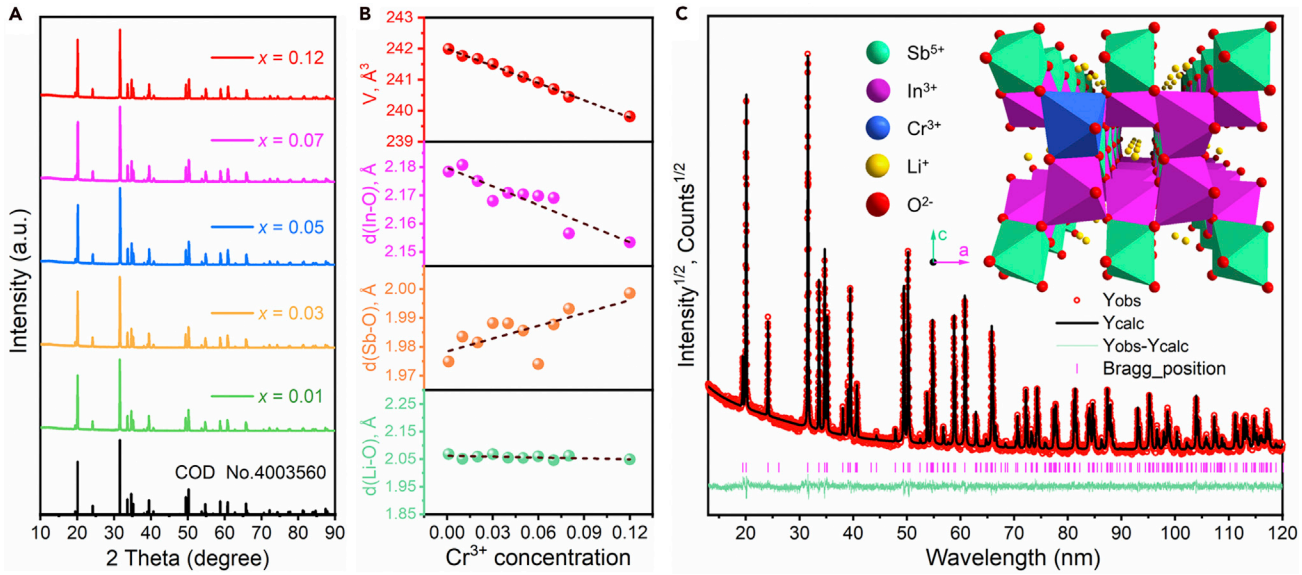

Figure 1. Crystal phase and structural characterization of $LiIn_2SbO_6$:Cr^{3+}

(A) XRD patterns of $LiIn_{2-x}SbO_6$: xCr^{3+} (x = 0 - 0.12) and the standard data of $LiIn_2SbO_6$ phase (COD No. 4003560).

(B) Variation of cell volume, In-O, Sb-O, and Li-O bond lengths with the increase of Cr^{3+} concentration, respectively.

(C) Rietveld refinement XRD pattern of $LiIn_{1.97}SbO_6$:$0.03Cr^{3+}$. The inset illustrates the substitute model of Cr^{3+} in $LiIn_2SbO_6$ host.

example, the luminous efficiency of $Ca_3Sc_2Si_3O_{12}$:Cr^{3+} under the excitation of 460 nm blue light can reach 92.3% with an exceptional thermal stability (Jia et al., 2020). The increase of the lattice parameters in Cr^{3+}-doped $X_3Sc_2Ga_3O_{12}$ (X = Lu, Y, Gd, La) can give rise to a red shift of emission band from 722 nm to 818 nm (Malysa et al., 2018). Furthermore, Rajendran et al. reported the ultra-broadband emission of $La_3Ga_5GeO_{14}$:Cr^{3+} phosphor with a FWHM of 330 nm (Rajendran et al., 2018; Zhao et al., 2020), and He et al. and Yao et al. improved the luminous efficiency, thermal resistance, and FWHM of $Ca_2LuZr_2Al_3O_{12}$:Cr^{3+} and $LiScP_2O_7$:Cr^{3+} phosphors by Yb^{3+} co-doping, respectively (He et al., 2020; Yao et al., 2020). However, the emission spectra of most NIR phosphors activated by Cr^{3+} ions have a considerable part in the visible light range (650-780 nm), which has inferior permeability to biotissues compared with long-wavelength NIR light and will cause irritation to naked eyes. As we know, only $LiNbO_3$:Cr^{3+} and $Cs_2AgInCl_6$:Cr^{3+} can achieve completely invisible fluorescence but cannot be pumped efficiently by the blue LED chips (Torchia et al., 2001; Zhao et al., 2019). Therefore, the development of long-wavelength ultra-broadband NIR phosphors that can be excited by blue LEDs is a challenging and far-reaching task. For example, we developed $MgTa_2O_6$:Cr^{3+} phosphor with an asymmetrical emission band ranging from 700 nm to 1150 nm and a large FWHM of 140 nm upon 460 nm blue light excitation, which matched LED applications (Liu et al., 2020a, 2020b).

In the present study, Cr^{3+}-doped $LiIn_2SbO_6$ phosphors are firstly designed and synthesized. Under 492-nm irradiation, $LiIn_{1.97}SbO_6$:$0.03Cr^{3+}$ shows a broader emission band covering from 780 nm to 1400 nm with a FWHM of 225 nm. The introduction of Na^+ on Li^+ sites induced a tunable emission spectrum and corresponding mechanism is discussed. After Yb^{3+} was co-doped with Cr^{3+} ions, an efficient NIR radiation of Yb^{3+} emitters with great thermal stability occurs upon 492-nm excitation and attributed to the energy transfer from Cr^{3+} to Yb^{3+} ions. The feasibility of $LiIn_{1.82}SbO_6$:$0.03Cr^{3+}$, $0.15Yb^{3+}$ phosphor for non-destructive biological monitoring and safety inspection applications is also investigated.

RESULTS AND DISCUSSION

Crystal structure and optical properties of $LiIn_{2-x}SbO_6$: xCr^{3+} (x = 0 - 0.12)

The X-ray diffraction (XRD) patterns of as-prepared $LiIn_{2-x}SbO_6$:xCr^{3+} (x = 0 - 0.12) samples are shown in Figure 1A, and the corresponding reference data are taken from the Crystallography Open Database (COD No.4003560). Obviously, all diffraction peaks can be assigned to the standard data of the $LiIn_2SbO_6$ phase, indicating the successful phase formation and Cr^{3+} doping. To obtain detailed

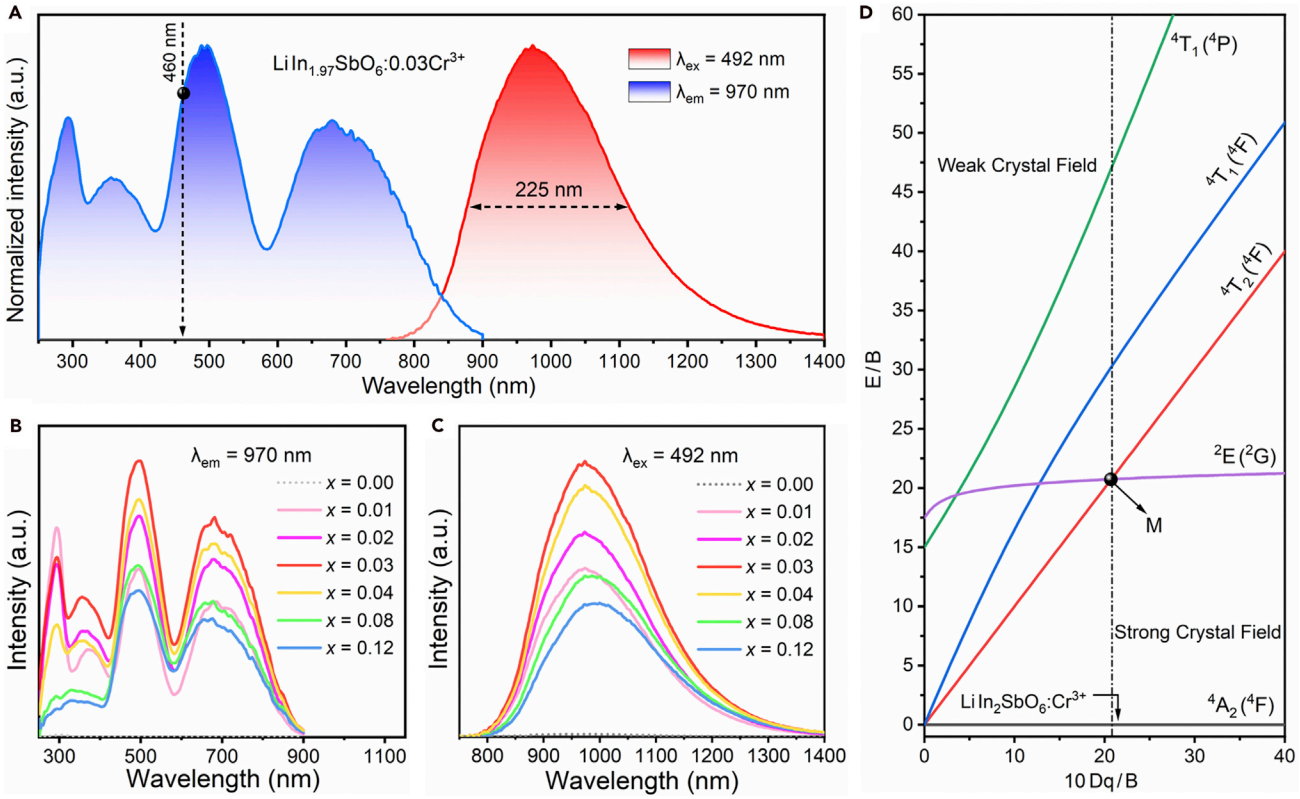

Figure 2. Photoluminescence spectra and crystal field strength of $LiIn_{2-x}SbO_6:xCr^{3+}$ (x = 0 - 0.12)

(A) Room temperature PLE (blue) and PL (red) spectra of $LiIn_{1.97}SbO_6:0.03Cr^{3+}$ phosphor. The dotted line labeled 460 nm means that the phosphor can be well excited by the commercial InGaN blue chips.

(B and C) Room temperature PLE and PL spectra of $LiIn_{2-x}SbO_6:xCr^{3+}$ (x = 0 - 0.12) phosphor, respectively.

(D) Tanabe-Sugano energy level diagram for Cr^{3+} ions ($3d^3$) in octahedral coordination. The point of M (10 D_q/B = 23) means the intersection of ^2E and $^4T_2$ (^4F) energy levels and the division of weak and strong crystal field.

crystallographic information, Rietveld refinement was performed by *TOPAS 4.2* software, and the results are displayed in Figures 1B and 1C (Bruker and Topas, 2008). It is notable that both the cell volume V and the average In-O bond length d(In-O) decrease linearly but the average Sb-O bond length d(Sb-O) increases with increasing Cr^{3+} concentration, which is in good agreement with the fact that the effetive ion radius of Cr^{3+} (0.62 Å when CN = 6) is much smaller than that of In^{3+} (0.80 Å when CN = 6) but slightly bigger than that of Sb^{5+} (0.60 Å when CN = 6) (Shannon, 1976). Therefore, it is reasonable to conclude that Cr^{3+} replaces In^{3+} and Sb^{5+} simultaneously in $LiIn_2SbO_6$ host. However, Cr^{3+} ions occupying In^{3+} sites should be the main mechanism in view of the charge balance and the absence of impure phase, as well as the lattice totally shrinks after Cr^{3+} was doped. Furthermore, the increase of d(Sb-O) may also be caused by the typical adjacent polyhedron substitution effect, which means that the doping of Cr^{3+} at In^{3+} sites will increase the strain of In-O bonds so that the O-Sb distance will increase to release this strain (Li et al., 2014). Nevertheless, this effect has minor influence on LiO_4 coordination polyhedron with smaller volume because the average bond length d(Li-O) remains almost unchanged with x increases.

Figure 1C shows the Rietveld refinement result of $LiIn_{1.97}SbO_6:0.03Cr^{3+}$ with satisfactory residual factors R_{wp} = 6.66%, R_p = 5.08%, R_B = 1.05%, and χ^2 = 3.73%. The detailed parameters are listed in Tables S1 and S2, which emphasizes the purity of target phase and the rutile-related lattice structure with a space group of *Pnnm* (Flynn et al., 2020). The inset in Figure 1C shows the substitute model of Cr^{3+} in $LiIn_2SbO_6$ host that formed by edge-sharing InO_6 and SbO_6 octahedrons while Li^+ ions are located at channels and play a role in balancing charge. Such open three-dimensional (3D) tunnel frameworks allow a good flexibility in composition and performance regulation as discussed later.

The fundamental luminescence properties of $LiIn_{1.97}SbO_6$:$0.03Cr^{3+}$ were investigated using the photoluminescence (PL) and PL excitation (PLE) spectra as shown in Figure 2A. Under 492-nm irradiation, the sample exhibits an ultra-broad NIR emission band peaking at 970 nm and extending from 780 nm to 1400 nm with a satisfactory FWHM of 225 nm. Furthermore, a continuous PLE spectrum composed of four peaks can be acquired when monitoring at the emission maximum. The first band centered at 294 nm may originate from the charge transfer (CT) from O ligands to central Sb atoms in the SbO_6 octahedral groups, and the others peaking at 360, 492, and 700 nm should be assigned to the $^4A_2 \rightarrow {}^4T_1$ (^4P), $^4A_2 \rightarrow {}^4T_1$ (^4F), and $^4A_2 \rightarrow {}^4T_2$ (^4F) energy level transitions of Cr^{3+} ions, respectively (Li et al., 2015; Mao et al., 2020). Clearly, $LiIn_{1.97}SbO_6$: $0.03Cr^{3+}$ phosphor can be pumped by the most efficient InGaN blue light chips (460 nm), as verified from the emission spectrum monitored by the 492-nm excitation. It is worth noting that the phosphor also exhibits the similar NIR spectrum under 294-nm excitation (Figure S1), which may be attributed to the energy transfer process (ET_1) from the CT band (CTB) to the excited energy level of Cr^{3+} as confirmed by the PLE spectra of $LiIn_{2-x}SbO_6$: $x\,Cr^{3+}$ (x = 0 - 0.12) as shown in Figure 2B. It is obvious that the $LiIn_2SbO_6$ host shows no fluorescence but a strong CT absorption peaked at 294 nm in its ultraviolet-visible-near infrared (UV-VIS-NIR) diffuse reflectance spectrum (Figure S2). After 0.01 Cr^{3+} was doped, the 294-nm excitation band appeared along with the three energy level transitions of Cr^{3+} ions when monitoring at 970 nm, indicating that the energy absorbed by $LiIn_{2-x}SbO_6$: xCr^{3+} was transferred to Cr^{3+} emitters. With the further increase of Cr^{3+} content, the intensity of CT excitation band in Figure 2B began to decrease which was mainly caused by the cross-relaxation process between Cr^{3+} ions so that certain excitation energy is consumed. The influence of Cr^{3+} concentration on the emission properties of $LiIn_{2-x}SbO_6$: xCr^{3+} (x = 0 - 0.12) is presented in Figure 2C. Obviously, the PL intensity reaches its maximum when x is 0.03, and then, the concentration quenching effect occurs (Yu et al., 2019). Therefore, $LiIn_{1.97}SbO_6$:$0.03Cr^{3+}$ is selected as the optimum composition for further characterizations.

As is known that the valence electrons of Cr^{3+} ions are not shielded by outer shells, there are strong interactions with the crystal field and lattice vibrations due to the spatial extension of the d electron wavefunctions in crystals, and thus it enables tunable optical properties of Cr^{3+} doped phosphors (Malysa et al., 2018). When considering Cr^{3+} ions in the center of coordinated octahedrons (O_h symmetry), the influence of the host lattice on luminescence properties can be expressed by the spectroscopic parameters of D_q, B, and β, which can be roughly estimated by the following equations (Tanabe and Sugano, 1954):

$$10\,D_q = E(^4T_2) = E(^4A_2 \rightarrow {}^4T_2) \qquad \text{(Equation 1)}$$

$$B = D_q \frac{x^2 - 10x}{15(x-8)} \qquad \text{(Equation 2)}$$

where parameter x is defined as follows:

$$x = E\frac{(^4T_1) - E(^4T_2)}{D_q} = E(^4A_2 \rightarrow {}^4T_1) - E(\frac{^4A_2 \rightarrow {}^4T_2)}{D_q} \qquad \text{(Equation 3)}$$

$$\beta = \frac{B}{B_0} \qquad \text{(Equation 4)}$$

In the above equations, D_q is the crystal field strength and closely related to the metal-ligand distance, $E(^4T_2)$ and $E(^4T_1)$ are the equilibrium positions of the $^4T_1$ and $^4T_2$ levels, and $E(^4A_2 \rightarrow {}^4T_2)$ and $E(^4A_2 \rightarrow {}^4T_1)$ represent the corresponding transition energies which can be obtained from the PLE spectrum of $LiIn_{1.97}SbO_6$:$0.03Cr^{3+}$ (Figure 2A). The Racah parameter B represents the repulsive force between electrons in the 3d orbital. The value for free Cr^{3+} ions (B_0 = 918 cm^{-1}) is much higher than that of Cr^{3+} in crystals, and their ratio β is often used to evaluate the covalency of host which varies in a more complex manner on interionic distances and the chemical nature of the ions (Malysa et al., 2018). The value of x is calculated from the energy differences between $^4A_2 \rightarrow {}^4T_1$ (^4F) and $^4A_2 \rightarrow {}^4T_2$ (^4F) transitions. The crystal field parameter D_q/B and is finally determined to be 2.32 for $LiIn_{1.97}SbO_6$:$0.03Cr^{3+}$ (Figure 2D) and slightly bigger than Cr^{3+} in weak crystal field ($D_q/B < 2.3$) in which a broad emission band appears (De Guzman et al., 2020). This inconsistency is not uncommon in certain oxide materials as shown in Table S3, which may be ascribed to the distortion of coordinate polyhedron (Figure S3) since the classical Tanabe-Sugano diagram is based on Cr^{3+} in a nearly perfect octahedral site (Mao et al., 2020; Henderson and Imbusch, 1989).

To investigate the detailed luminescence mechanism of $LiIn_{1.97}SbO_6$:$0.03Cr^{3+}$, temperature-dependent PL spectra and fluorescence decay curves were recorded in Figures 3A and 3B, respectively. Apparently,

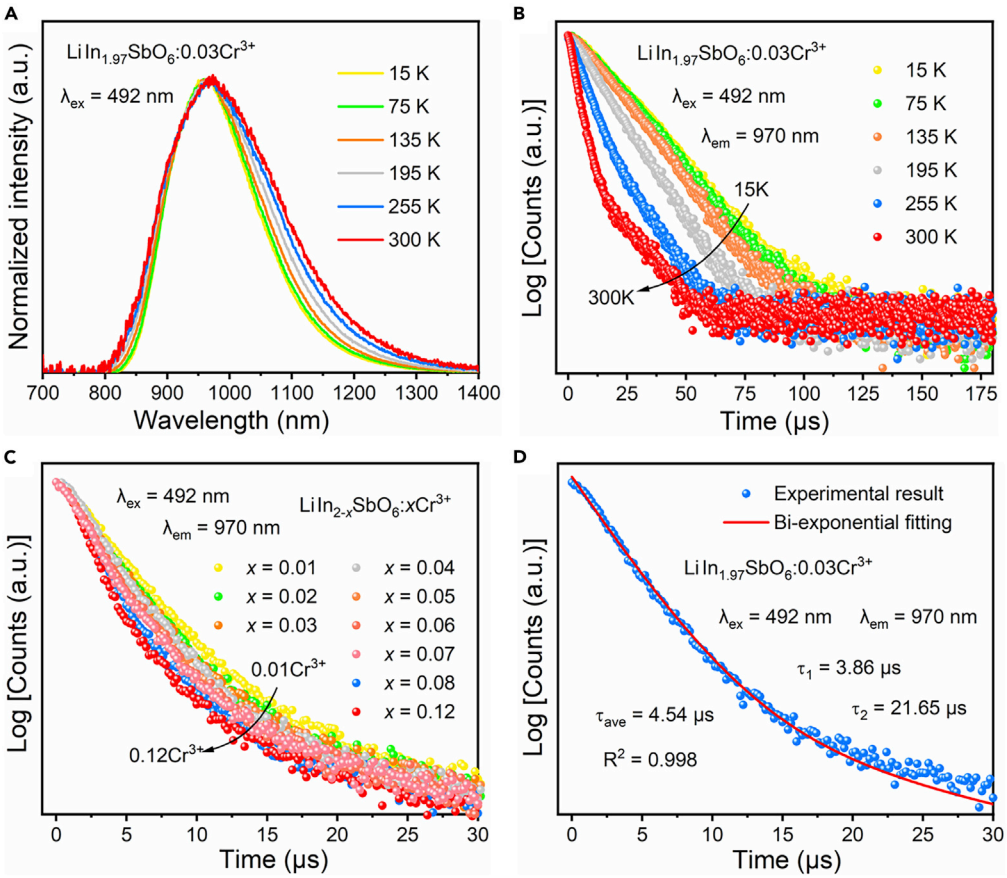

Figure 3. Temperature-dependent PL spectra and fluorescence decay curves of $LiIn_{2-x}SbO_6:xCr^{3+}$ ($x = 0.01 - 0.12$)

(A and B) Normalized temperature-dependent PL spectra and fluorescence decay curves of $LiIn_{1.97}SbO_6:0.03Cr^{3+}$ under 492-nm excitation between 15 and 300 K, respectively.

(C) Room temperature fluorescence decay curves of $LiIn_{2-x}SbO_6:xCr^{3+}$ (x = 0.01–0.12) monitored at 970 nm upon excitation at 492 nm.

(D) Bi-exponential fitting of room temperature fluorescence decay curves for $LiIn_{1.97}SbO_6:0.03Cr^{3+}$.

the PL intensity gradually declines (Figure S4) but is broadened significantly (~50 nm, Figure 3A) as the temperature increases, which should be ascribed to the temperature-induced enhancement of electron-phonon interactions (Zhao et al., 2019). Furthermore, the fluorescence decay curve of $LiIn_{1.97}SbO_6:0.03Cr^{3+}$ is close to mono-exponential at 15 K but bi-exponential at 300 K (Figure 3B), which may be caused by the introduction of additional energy decay paths at high temperature like cross-relaxation, energy migration, or the defect-induced non-radiative relaxation process (Yu et al., 2019; Bachmann et al., 2009). The shortening of lifetime with the increase of temperature and Cr^{3+} content (Figure 3C) could be the evidence of temperature quenching and concentration quenching effect, respectively. The bi-exponential fitting of room temperature fluorescence decay curves for $LiIn_{1.97}SbO_6:0.03Cr^{3+}$ is shown in Figure 3D. The average lifetime was calculated to be 4.54 μs based on the following relationships:

$$I = A_1 e^{-\frac{t}{\tau_1}} + A_2 e^{-\frac{t}{\tau_2}} \quad \text{(Equation 5)}$$

$$\tau_{ave} = \frac{A_1\tau_1^2 + A_2\tau_2^2}{A_1\tau_1 + A_2\tau_2} \quad \text{(Equation 6)}$$

where I represents the emission intensity, A_1 and A_2 are constants, τ_1 and τ_2 are the decay time for the exponential components, and τ_{ave} is the average decay time. The fitting results ($\tau_1 = 3.86$ μs and $\tau_2 = 21.65$ μs) are in line with the typical Cr^{3+}-doped compounds, and the shorter one is regarded as intrinsic ionic luminescence when the influence of temperature is taken into consideration (Gao et al., 2020).

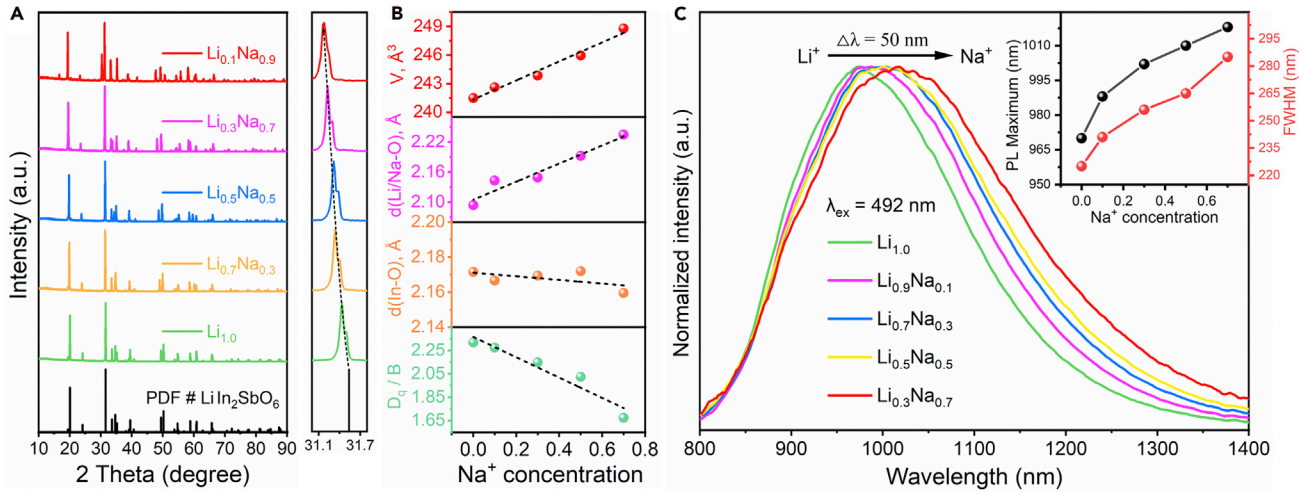

Figure 4. Rietveld refinement and fluorescence spectra of $(Li_{1-z}Na_z)In_{1.97}SbO_6:0.03Cr^{3+}$ (z = 0 - 0.9)

(A) XRD patterns of $(Li_{1-z}Na_z)In_{1.97}SbO_6:0.03Cr^{3+}$ (z = 0 - 0.9).

(B) Variation of cell volume, Li/Na-O bond length, In-O bond length, and crystal field parameter D_q/B with the increase of Na^+ concentration, respectively.

(C) The influence of Na^+ concentration on the emission spectra of $(Li_{1-z}Na_z)In_{1.97}SbO_6:0.03Cr^{3+}$ (z = 0 - 0.7). The inset displays the PL maximum and FWHM as a function of Na^+ concentration.

PL broadening by local structure regulation

According to the Tanabe-Sugano diagram shown in Figure 2D, the emission spectrum of Cr^{3+} ions in the center of coordinated octahedrons is closely related to surrounding crystal field. Generally, the ion substitution strategy is considered as an effective way to regulate the local structure and crystal field distortion so that a great change in the emission spectrum will take place (Chen et al., 2017). In addition, the Li^+ ions in $LiIn_2SbO_6$ (0.59 Å when CN = 4) are located at unique channels and play a role in charge balance, which determine that it can be replaced by equivalent ions conveniently. Therefore, Na^+ ions with larger effetive radius (0.99 Å when CN = 4) were introduced into this host with a certain stoichiometric $Li_{1-x}Na_xIn_{1.97}SbO_6:0.03Cr^{3+}$ (x = 0 - 0.9), and their XRD patterns are shown in Figure 4A. No impurity patterns have been detected even in the case of x = 0.7, and it reveals that the regulated phosphors keep the same crystal structure as $LiIn_2SbO_6$. The inset demonstrates the shift of the strongest diffraction peak toward lower angle side, suggesting that the crystal lattice expands gradually with the increase of Na^+ content, which is further verified by the variations of cell volume and average Li/Na-O bond length obtained by Rietveld refinement (Figure 4B). After Na^+ was introduced, both of them increase linearly, and the PL spectrum of Cr^{3+} can be tuned from 970 nm to 1020 nm with considerable broadening of FWHM (~60 nm) (Figures 4C and S5). According to the excitation spectra of $Li_{1-x}Na_xIn_{1.97}SbO_6:0.03Cr^{3+}$ (x = 0 - 0.7) shown in Figure S5, the calculated crystal field strength D_q almost unchanged which is in line with their average In-O bond length (Figure 4B), while Racah parameter B increase significantly from 616 cm^{-1} to 854 cm^{-1} means a reduction of host covalency and consists with the change of average Li/Na-O bond length (Malysa et al., 2018; Malysa et al., 2017). Finally, the crystal field parameter D_q/B is decreased from 2.32 to 1.67 as displayed in Figure 4B and Table S4. This tunable long-wavelength NIR fluorescence is closely associated with the crystallographic parameters of the host that are governed by alkali metal ions in this open 3D tunnel framework and will take an avenue to broaden the research direction and application prospects of NIR fluorescence materials.

Yb^{3+} co-doping enabling increased PL intensities and enhanced thermal stability

Yb^{3+} ions are considered as ideal spectral converters, especially coupling with other lanthanide ions, for their NIR emission and efficient pumping by 980-nm laser. Inspired by the possible energy transfer between Cr^{3+} and Yb^{3+} ions, as well as the closed effetive ion radius of Yb^{3+} (0.87 Å when CN = 6) to In^{3+} (0.80 Å when CN = 6), Cr^{3+} and Yb^{3+} co-doped phosphors were developed to further improve its application potential. It can be seen in Figure 5A that after Yb^{3+} was doped singly, the sample can still exhibit strong NIR fluorescence under excitation at 294 nm, indicating that there is another ET process (ET_2) between CTB and the Yb^{3+} excited state energy level in the phosphor. When Yb^{3+} was co-doped with Cr^{3+}, the emission spectrum changes from the broadband emission of Cr^{3+} to the sharp line emission of Yb^{3+}, while the shape and position of the excitation spectrum of $LiIn_{1.82}SbO_6:0.03Cr^{3+}$, $0.15Yb^{3+}$ remains

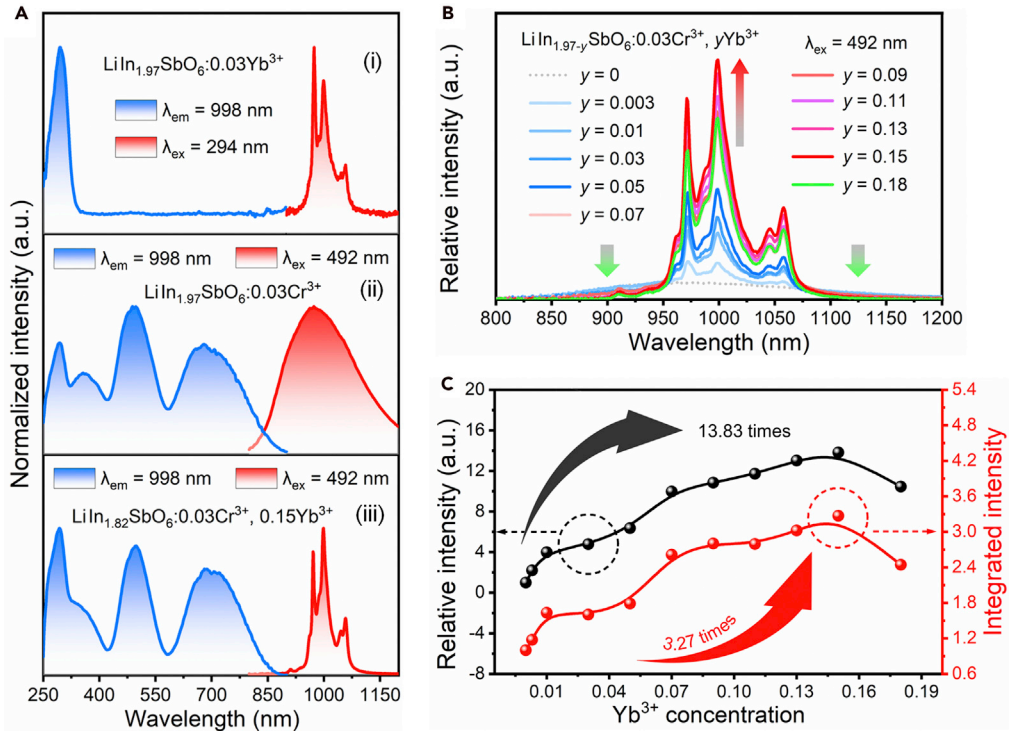

Figure 5. Fluorescence spectra of $LiIn_{1.97-y}SbO_6$:0.03Cr^{3+}, yYb^{3+} (y = 0 - 0.18)

(A) Room temperature PLE (blue) and PL (red) spectra of $LiIn_{1.97}SbO_6$:0.03Yb^{3+}, $LiIn_{1.97}SbO_6$:0.03Cr^{3+}, and $LiIn_{1.82}SbO_6$:0.03Cr^{3+}, 0.15Yb^{3+} phosphors.

(B) PL spectra of $LiIn_{1.97-y}SbO_6$:0.03Cr^{3+}, yYb^{3+} (y = 0 - 0.18) phosphors under 492-nm excitation.

(C) The relative and integrated emission intensity of $LiIn_{1.97-y}SbO_6$:0.03Cr^{3+}, yYb^{3+} (y = 0 - 0.18) phosphors as a function of Yb^{3+} concentration.

basically unchanged compared with $LiIn_{1.97}SbO_6$:0.03Cr^{3+} except that the 294-nm excitation band was further enhanced due to the additional ET_2 process, indicating that there is the third ET process (ET_3) from Cr^{3+} to Yb^{3+} ions. This process was confirmed by the emission spectra of $LiIn_{1.97-y}SbO_6$:0.03Cr^{3+}, yYb^{3+} (y = 0 - 0.18) as shown in Figure 5B. The emission intensity of Cr^{3+} located at 900 nm and 1150 nm decreases monotonously while the luminescence of Yb^{3+} at 998 nm increases rapidly with the increase of Yb^{3+} content, which should be attributed to the enhancement of ET_3. The emission of Yb^{3+} upon 492-nm excitation starts to decrease when $y > 0.15$ due to the shortening of the distance among Yb^{3+} ions so that the concentration quenching effect occurs. In this process, the relative and integrated emission intensity of co-doped sample can be improved up to 13.83 times and 3.27 times, respectively, even if the emission bandwidth is narrowed significantly compared with $LiIn_{1.97}SbO_6$:0.03Cr^{3+}, as indicated in Figure 5C. This remarkable enhancement of PL intensity should be attributed to the efficient ET_3 and Yb^{3+} emitters in the co-doped samples, which was characterized through the change of fluorescence lifetime of Cr^{3+} and Yb^{3+} as shown in Figures 6A and 6B. Upon 492-nm excitation, both of Cr^{3+} and Yb^{3+} show emission at $\sim$ 1000 nm so that the decay curves of $LiIn_{1.97-y}SbO_6$:0.03Cr^{3+}, yYb^{3+} (y = 0 - 0.18) actually stem from the joint contributions of their luminescence. Through the bi-exponential fitting for the fluorescence decay curves of co-doped samples (Figure S6), the specific lifetime values of Cr^{3+} in each sample was obtained and depicted in Figure 6B (black line), and then, the ET efficiency (η_{ET}) from Cr^{3+} to Yb^{3+} can be calculated based on Equation 7:

$$\eta_{ET} = 1 - \frac{\tau}{\tau_0} \quad \text{(Equation 7)}$$

where τ and τ_0 are the corresponding decay times of Cr^{3+} in the presence and absence of Yb^{3+}, respectively. According to the above fitted lifetimes, the ET efficiency in $LiIn_{1.84}SbO_6$:0.03Cr^{3+}, 0.13Yb^{3+} reached above 80% and will be further enhanced for higher Yb^{3+} concentration samples. This efficient ET_3 process may be ascribed to two main reasons: on the one hand, Cr^{3+} and Yb^{3+} ions both occupy the In^{3+} sites in

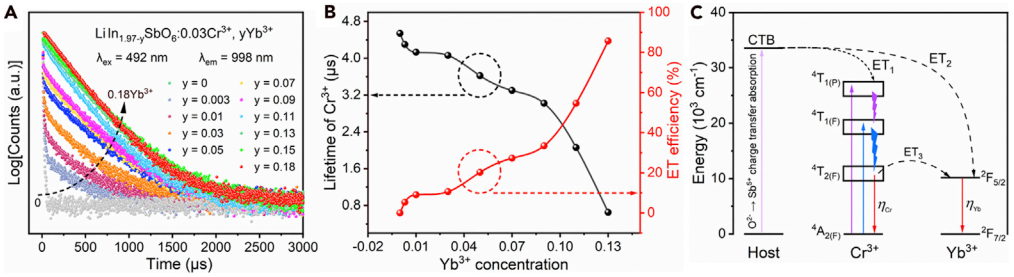

Figure 6. Fluorescence decay curves and energy transfer process

(A) Room temperature fluorescence decay curves of $LiIn_{1.97-y}SbO_6$:0.03Cr^{3+}, yYb^{3+} (y = 0 - 0.18) phosphor under 492-nm excitation and monitored at 998 nm.

(B) The lifetime of Cr^{3+} and the ET efficiency from Cr^{3+} to Yb^{3+} as a function of Yb^{3+} concentration in $LiIn_2SbO_6$ host.

(C) Schematic diagram of energy level and energy transfer processes in $LiIn_{1.82}SbO_6$:0.03Cr^{3+}, 0.15Yb^{3+} phosphor.

$LiIn_2SbO_6$ host, and the shorter distance between activators and sensitizers is conducive to the occurrence of ET_3 process. On the other hand, the maximum emission wavelength of Cr^{3+} ions is quite close to the absorption of Yb^{3+} ions in $LiIn_2SbO_6$, indicating that there is a tiny energy difference between Cr^{3+} and Yb^{3+} excited state energy level and a slight relaxation will facilitate the transfer of energy. The schematic diagram of three ET processes in $LiIn_{1.82}SbO_6$:0.03Cr^{3+}, 0.15Yb^{3+} phosphor is demonstrated in Figure 6C, and the specific positions of each energy level were calculated through the corresponding transition energy in Figure 5A. The three basic energy transfer processes ET_1, ET_2 and ET_3 originate from the CTB to Cr^{3+}, the CTB to Yb^{3+} and Cr^{3+} to Yb^{3+} excited state energy level, respectively. It is clear that the energy difference of ET_3 is so inappreciable that this process will happen significantly and may improve luminescence intensity by over an order of magnitude.

In order to evaluate the thermal stability and temperature-quenching mechanisms of $LiIn_{1.97}SbO_6$:0.03Cr^{3+} and $LiIn_{1.82}SbO_6$:0.03Cr^{3+}, 0.15Yb^{3+}, PL/temperature correlation maps of the two phosphors upon 492-nm excitation were measured as shown in Figures 7A and 7B, respectively. Apparently, the thermal resistance of $LiIn_{1.82}SbO_6$:0.03Cr^{3+}, 0.15Yb^{3+} (31% @ 95°C) is much better than that of $LiIn_{1.97}SbO_6$:0.03 Cr^{3+} (10% @ 95°C) upon 492-nm excitation but worse than that of $LiIn_{1.97}SbO_6$:0.03Yb^{3+} (95% @ 95°C) upon 980-nm laser excitation (Figure 7C), which can be explained by the typical configuration coordinate diagram in Figure 7D. Normally, the large stokes shift (3976 cm^{-1}) and low radiant energy (1.28 eV) are accompanied by a smaller activation energy E_a for Cr^{3+} ions in $LiIn_2SbO_6$ so that the non-radiative transition is quite serious (Yao et al., 2020). However, the temperature-quenching effect of Yb^{3+} mainly governed by the multi-phonon emission is smaller than the 5-fold vibration energy of the surrounding environment. Therefore, one can think that the Yb^{3+} in $LiIn_2SbO_6$ exhibits a satisfactory thermal resistance. Moreover, the reduced thermal quenching effect can be found in $LiIn_{1.82}SbO_6$:0.03Cr^{3+}, 0.15Yb^{3+} in view of the efficient ET_3 from Cr^{3+} to thermally more stable Yb^{3+} ions other than non-radiative process.

Quantum efficiency and non-invasive detection application

The quantum efficiency (QE) of $LiIn_{1.97}SbO_6$:0.03Cr^{3+} and $LiIn_{1.82}SbO_6$:0.03Cr^{3+}, 0.15Yb^{3+} phosphors is measured to evaluate their luminescence properties as shown in Figure S7. The relatively low internal (7%) and external (3.44%) QEs of $LiIn_{1.97}SbO_6$:0.03Cr^{3+} are attributed to the serious non-radiation relaxation process and parity-forbidden transition of Cr^{3+} ions, respectively. Given that the $LiIn_{1.82}SbO_6$:0.03Cr^{3+}, 0.15Yb^{3+} phosphor shows a stronger NIR fluorescence than $LiIn_{1.97}SbO_6$:0.03Cr^{3+} under 492-nm excitation, an NIR pc-LED was fabricated by coating the $LiIn_{1.82}SbO_6$:0.03Cr^{3+}, 0.15Yb^{3+} phosphor on a commercial blue light-emitting InGaN chip (460 nm) to evaluate the potential practical application of the NIR luminescence material. Figure 8 demonstrates the schematic diagram of NIR pc-LED imaging device showing the application principle. Some details are shown in this figure. Firstly, one can fabricate the NIR pc-LED based on $LiIn_{1.82}SbO_6$:0.03Cr^{3+}, 0.15Yb^{3+} phosphor, and the driven current-dependent emission spectra and operating temperature of the fabricated NIR pc-LED are shown in Figure S8. Under the optimal driven current of 40 mA, the NIR fluorescence of the light source can penetrate ~ 2 cm pork tissue so that a nail behind this tissue and the insertion depth of a needle can be observed through smart networking devices such as mobile phones and computers with the assistance of an NIR camera, as given in the inset of Figure 8. These

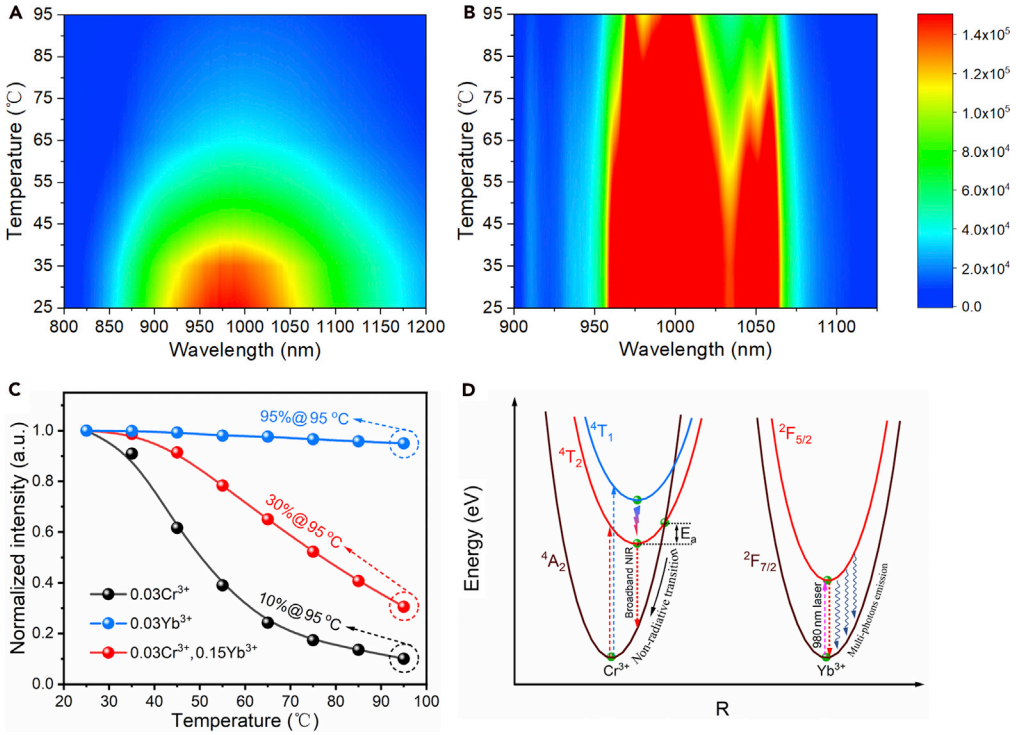

Figure 7. Temperature-dependent PL intensity and temperature-quenching mechanism

(A and B) PL/temperature correlation maps of $LiIn_{1.97}SbO_6$:0.03Cr^{3+} and $LiIn_{1.82}SbO_6$:0.03Cr^{3+}, 0.15Yb^{3+} upon 492-nm excitation, respectively.

(C) The normalized PL intensity of $LiIn_{1.97}SbO_6$:0.03Yb^{3+} under 980 nm laser as a function of temperature, as well as $LiIn_{1.97}SbO_6$:0.03Cr^{3+} and $LiIn_{1.82}SbO_6$:0.03Cr^{3+}, 0.15Yb^{3+} upon 492-nm excitation.

(D) Configuration coordinate diagrams of Cr^{3+} and Yb^{3+} showing temperature-quenching mechanism of $LiIn_{1.82}SbO_6$:0.03Cr^{3+}, 0.15Yb^{3+} phosphor.

images with a fundamental model indicate that the phosphor will be potentially applied in accurate measurements of non-destructive examination.

Conclusion

In summary, we have developed a broadband NIR phosphor by introducing Cr^{3+} ions in $LiIn_2SbO_6$ host, and the $LiIn_2SbO_6$:Cr^{3+} phosphors exhibit NIR emissions in the range 780-1400 nm with an FWHM of ~225 nm. The open 3D tunnel framework of $LiIn_2SbO_6$ allows a good flexibility in composition so that the emission maximum can be tuned from 970 nm to 1020 nm together with broadened FWHM of ~285 nm by substituting Li^+ with Na^+ gradually, which mainly attributed to the weakening of crystal field from D_q/B = 2.32 to 1.67. When Yb^{3+} ions were co-doped with Cr^{3+} in $LiIn_2SbO_6$, the PL intensity of Cr^{3+} was suppressed but a stronger narrow-band NIR peak of Yb^{3+} (more over 13 times of $LiIn_{1.97}SbO_6$:0.03Cr^{3+}) appeared under 492 nm excitation. Spectroscopic and lifetime analysis shows that this enhancement is mainly due to efficient energy transfer from Cr^{3+} to more efficient and thermally stable Yb^{3+} emitters. Finally, an NIR pc-LED is fabricated by $LiIn_{1.82}SbO_6$:0.03 Cr^{3+}, 0.15Yb^{3+} phosphor and an InGaN blue chip peaking at 460 nm. The result demonstrates that a nail inside pork tissues (~2 cm) and the insertion depth of a needle can be observed, indicating that the as-fabricated NIR pc-LED based on NIR phosphor can be applied in the field of non-destructive detection and also provide new insights for the design of new NIR materials for LED applications.

Limitations of the study

The thermal stabilities and quantum efficiency of the Cr^{3+}-activated or Cr^{3+}-Yb^{3+}-doped $LiIn_2SbO_6$ NIR phosphors should be especially followed with interests and improved for the practical applications.

A commercial InGaN blue chip with the peak at 460 nm was used to fabricate the NIR pc-LED for the lack of 492-nm chip.

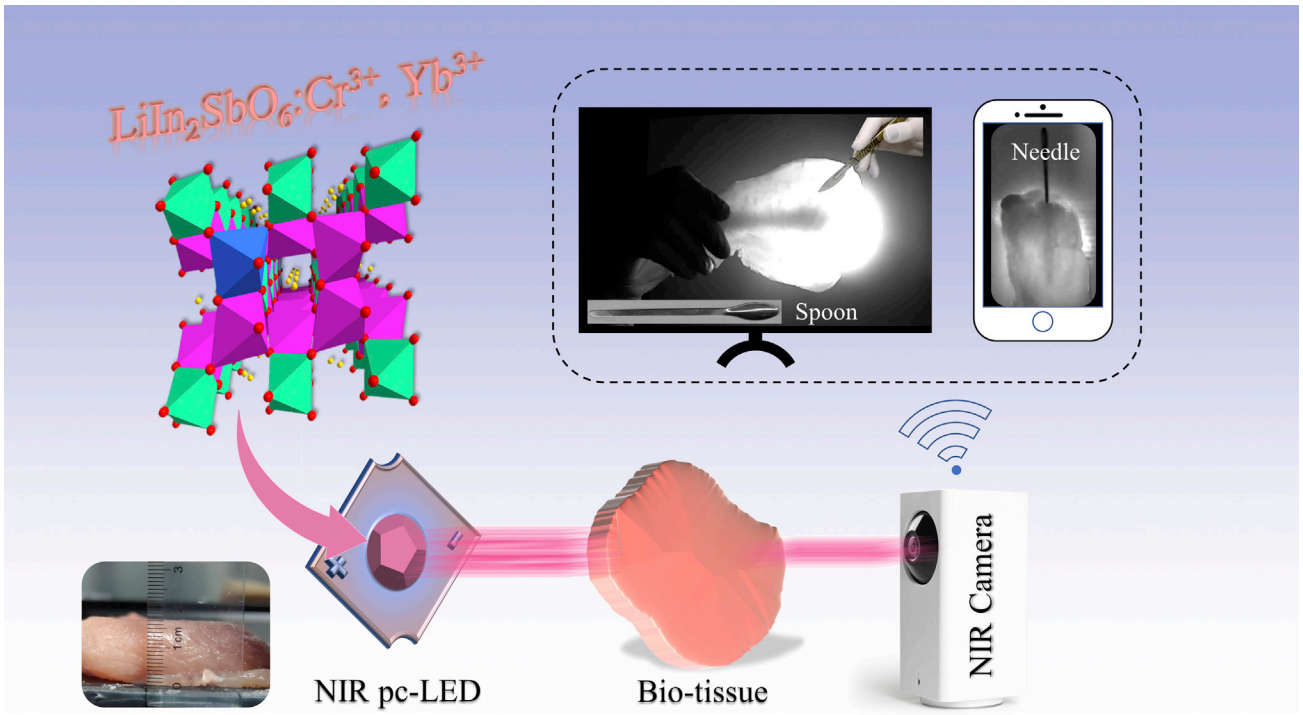

Figure 8. Schematic diagram of NIR pc-LED imaging device showing the application principle

METHODS

All methods can be found in the accompanying transparent methods supplemental file.

SUPPLEMENTAL INFORMATION

Supplemental information can be found online at https://doi.org/10.1016/j.isci.2021.102250.

ACKNOWLEDGMENTS

The present work was supported by the National Natural Science Foundation of China of China (Grant Nos. 51972118 and 51961145101), the Fundamental Research Funds for the Central Universities (D2190980), the Guangzhou Science & Technology Project (202007020005), the Local Innovative and Research Teams Project of Guangdong Pearl River Talents Pro-gram (2017BT01X137), and RFBR according to the research project No. 19-52-80003.

AUTHOR CONTRIBUTIONS

Z.X. conceived the project, revised the paper, and was primarily responsible for the experiment. G.L. synthesized the materials, performed experimental characterization, and wrote the paper. T.H. contributed the luminescence mechanism analysis. M.M performed the structure refinement. All authors contributed to the general discussion.

DECLARATION OF INTERESTS

The authors declare no competing interests.

Received: December 19, 2020
Revised: February 1, 2021
Accepted: February 25, 2021
Published: April 23, 2021

REFERENCES

Bachmann, V., Ronda, C., Oeckler, O., Schnick, W., and Meijerink, A. (2009). Color point tuning for $(Sr,Ca,Ba)Si_2O_2N_2:Eu^{2+}$ for white light LEDs. Chem. Mater. *21*, 316–325.

Bai, Q., Zhao, S., Guan, L., Wang, Z., Li, P., and Xu, Z. (2018). Design and control of the luminescence of Cr^{3+}-doped phosphors in the near-infrared I region by fitting the crystal field. Cryst. Growth Des. *18*, 3178–3186.

Berezovskaya, I.V., Dotsenko, V.P., Voloshinovskii, A.S., and Smola, S.S. (2013). Near infrared emission of Eu^{2+} ions in $Ca_3Sc_2Si_3O_{12}$. Chem. Phys. Lett. *585*, 11–14.

Cao, J., Xue, Y., Peng, J., Li, X., Huang, M., Xu, S., Yang, Z., and Peng, M. (2018). Enhanced NIR photoemission from Bi-doped aluminoborate glasses via topological tailoring of glass structure. J. Am. Ceram. Soc. *102*, 1710–1719.

Bruker, and Topas. (2008). General profile and structure analysis software for powder diffraction data, version 4 (Bruker AXS).

Cao, J., Peng, J., Wang, L., Luo, H., Wang, X., Xiong, P., Wang, Y., and Peng, M. (2019). Broadband NIR emission from multiple Bi centers in nitridated borogermanate glasses via tailoring local glass structure. J. Mater. Chem. C *7*, 2076–2084.

Chan, M.-H., Huang, W.-T., Wang, J., Liu, R.-S., and Hsiao, M. (2020). Next-generation cancer-specific hybrid theranostic nanomaterials: MAGE-A3 NIR persistent luminescence nanoparticles conjugated to afatinib for in situ suppression of lung adenocarcinoma growth and metastasis. Adv. Sci. *7*, 1903741.

Chen, M., Xia, Z., Molokeev, M.S., Lin, C.C., Su, C., Chuang, Y.-C., and Liu, Q. (2017). Probing Eu^{2+} luminescence from different crystallographic sites in $Ca_{10}M(PO_4)_7:Eu^{2+}$ (M = Li, Na, and K) with β-$Ca_3(PO_4)_2$-type structure. Chem. Mater. *29*, 7563–7570.

Fang, M.-H., Huang, P.-Y., Bao, Z., Majewska, N., Leśniewski, T., Mahlik, S., Grinberg, M., Leniec, G., Kaczmarek, S.M., Yang, C.-W., et al. (2020). Penetrating biological tissue using light-emitting diodes with a highly efficient near-infrared $ScBO_3:Cr^{3+}$ Phosphor. Chem. Mater. *32*, 2166–2171.

Flynn, S., Sanghvi, S., Matthew, K.J.G., Nisbet, L., Zhang, W., Shiv Halasyamani, P., Haile, S.M., and Poeppelmeier, K.R. (2020). $LiIn_2SbO_6$: a new rutile-related structure type with unique ion channels. Chem. Mater. *32*, 4785–4794.

Gao, T., Zhuang, W., Liu, R., Liu, Y., Chen, X., and Xue, Y. (2020). Design and control of the luminescence in Cr^{3+}-doped NIR phosphors *via* crystal field engineering. J. Alloys Compd. *848*, 156557.

Gong, X., Yang, Z., Walters, G., Comin, R., Ning, Z., Beauregard, E., Adinolfi, V., Voznyy, O., and Sargent, E.H. (2016). Highly efficient quantum dot near-infrared light-emitting diodes. Nat. Photon. *10*, 253–257.

Guan, W., Xiao, S., and Yang, X. (2020). Broadband-sensitive up-conversion phosphor of Ni^{2+},Tm^{3+} co-doped $LiGa_5O_8$. J. Lumin. *217*, 116795.

De Guzman, G.N.A., Fang, M.-H., Liang, C.-H., Bao, Z., Hu, S.-F., and Liu, R.-S. (2020). Near-infrared phosphors and their full potential: a review on practical applications and future perspectives. J. Lumin. *219*, 116944.

He, S., Zhang, L., Wu, H., Wu, H., Pan, G., Hao, Z., Zhang, X., Zhang, L., Zhang, H., and Zhang, J. (2020). Efficient super broadband NIR $Ca_2LuZr_2Al_3O_{12}:Cr^{3+},Yb^{3+}$ garnet phosphor for pc-LED light source toward NIR spectroscopy applications. Adv. Opt. Mater. *8*, 1901684.

Henderson, B., and Imbusch, G.F. (1989). Optical spectroscopy of inorganic solids (Oxford University).

Huang, W.-T., Yoon, S.-Y., Wu, B.-H., Lu, K.-M., Lin, C.-M., Yang, H., and Liu, R.-S. (2020). Ultra-broadband near-infrared emission $CuInS_2$/ZnS quantum dots with high power efficiency and stability for the theranostic applications of mini light-emitting diodes. Chem. Commun. *56*, 8285–8288.

Jia, Z., Yuan, C., Liu, Y., Wang, X.J., Sun, P., Wang, L., Jiang, H., and Jiang, J. (2020). Strategies to approach high performance in Cr^{3+}-doped phosphors for high-power NIR-LED light sources. Light Sci. Appl. *9*, 86.

Li, G., Lin, C.C., Chen, W.-T., Molokeev, M.S., Atuchin, V.V., Chiang, C.-Y., Zhou, W., Wang, C.-W., Li, W.-H., Sheu, H.-S., et al. (2014). Photoluminescence tuning *via* cation substitution in oxonitridosilicate phosphors: DFT calculations, different site occupations, and luminescence mechanisms. Chem. Mater. *26*, 2991–3001.

Li, K., Liu, X., Zhang, Y., Li, X., Lian, H., and Lin, J. (2015). Host-sensitized luminescence properties in $CaNb_2O_6:Ln^{3+}$ (Ln^{3+} = Eu^{3+}/Tb^{3+}/Dy^{3+}/Sm^{3+}) phosphors with abundant colors. Inorg. Chem. *54*, 323–333.

Liu, S., Wang, Z., Cai, H., Song, Z., and Liu, Q. (2020a). Highly efficient near-infrared phosphor $LaMgGa_{11}O_{19}:Cr^{3+}$. Inorg. Chem. Front. *7*, 1467–1473.

Liu, G., Molokeev, M.S., Lei, B., and Xia, Z. (2020b). Two-site Cr^{3+} occupation in the $MgTa_2O_6:Cr^{3+}$ phosphor toward broad-band near-infrared emission for vessel visualization. J. Mater. Chem. C *8*, 9322–9328.

Malysa, B., Meijerink, A., Wub, W., and Jüstel, T. (2017). On the influence of calcium substitution to the optical properties of Cr^{3+} doped $SrSc_2O_4$. J. Lumin. *190*, 234–241.

Malysa, B., Meijerink, A., and Jüstel, T. (2018). Temperature dependent Cr^{3+} photoluminescence in garnets of the type $X_3Sc_2Ga_3O_{12}$ (X = Lu, Y, Gd, La). J. Lumin. *202*, 523–531.

Mao, M., Zhou, T., Zeng, H., Wang, L., Huang, F., Tang, X., and Xie, R.-J. (2020). Broadband near-infrared (NIR) emission realized by the crystal-field engineering of $Y_{3-x}Ca_xAl_{5-x}Si_xO_{12}:Cr^{3+}$ (x = 0-2.0) garnet phosphors. J. Mater. Chem. C *8*, 1981–1988.

Małysa, B.M. (2019). Near infrared broad band emitting Cr^{3+} phosphors for pc-LEDs (Utrecht University).

Qiao, J., Zhou, G., Zhou, Y., Zhang, Q., and Xia, Z. (2019). Divalent europium-doped near-infrared-emitting phosphor for light-emitting diodes. Nat. Commun. *10*, 5267.

Rajendran, V., Fang, M.-H., Guzman, G.N.D., Lesniewski, T., Mahlik, S., Grinberg, M., Leniec, G., Kaczmarek, S.M., Lin, Y.-S., Lu, K.-M., et al. (2018). Super broadband near-infrared phosphors with high radiant flux as future light sources for spectroscopy applications. ACS Energy Lett. *3*, 2679–2684.

Shannon, R.D. (1976). Revised effective ionic radii and systematic studies of interatomie distances in halides and chaleogenides. Acta Cryst. *A32*, 751–767.

Song, E., Ye, S., Liu, T., Du, P., Si, R., Jing, X., Ding, S., Peng, M., Zhang, Q., and Wondraczek, L. (2015). Tailored near-infrared photoemission in fluoride perovskites through activator aggregation and super-exchange between divalent manganese ions. Adv. Sci. *2*, 1500089.

Song, E., Jiang, X., Zhou, Y., Lin, Z., Ye, S., Xia, Z., and Zhang, Q. (2019). Heavy Mn^{2+} doped $MgAl_2O_4$ phosphor for high-efficient near-infrared light-emitting diode and the night-vision application. Adv. Opt. Mater. *7*, 1901105.

Tan, Z.K., Moghaddam, R.S., Lai, M.L., Docampo, P., Higler, R., Deschler, F., Price, M., Sadhanala, A., Pazos, L.M., Credgington, D., et al. (2014). Bright light-emitting diodes based on organometal halide perovskite. Nat. Nanotechnol. *9*, 687–692.

Tanabe, Y., and Sugano, S. (1954). On the absorption spectra of complex ions II. J. Phys. Soc. Jpn. *9*, 766–779.

Tang, Z., Zhang, Q., Cao, Y., Li, Y., and Wang, Y. (2020). Eu^{2+}-doped ultra-broadband VIS-NIR emitting phosphor. Chem. Eng. J. *388*, 124231.

Tessler, N., Medvedev, V., Kazes, M., Kan, S., and Banin, U. (2002). Efficient near-infrared polymer nanocrystal light-emitting diodes. Science *295*, 1506–1508.

Torchia, G.A., Matos, O.M., Vaveliuk, P., and Tocho, J.O. (2001). Electron–lattice coupling in congruent Co-doped $LiNbO_3:Cr^{3+}$:ZnO crystal. J. Phys. Condensed Matter. *13*, 6577–6583.

Wang, C., Wang, X., Zhou, Y., Zhang, S., Li, C., Hu, D., Xu, L., and Jiao, H. (2019). An ultra-broadband near-infrared Cr^{3+}-activated gallogermanate $Mg_3Ga_2GeO_8$ phosphor as light sources for food analysis. ACS Appl. Electron. Mater. *1*, 1046–1053.

Wei, Y., Gao, Z., Yun, X., Yang, H., Liu, Y., and Li, G. (2020). Abnormal Bi^{3+}-activated NIR emission in highly symmetric $XAl_{12}O_{19}$ (X = Ba, Sr, Ca) by selective sites occupation. Chem. Mater. *32*, 8747–8753.

Xiong, P., Li, Y., and Peng, M. (2020). Recent advances in super broad infrared luminescence bismuth-doped crystals. iScience *23*, 101578.

Yao, L., Shao, Q., Han, S., Liang, C., He, J., and Jiang, J. (2020). Enhancing near-infrared photoluminescence intensity and spectral properties in Yb^{3+} codoped $LiScP_2O_7:Cr^{3+}$. Chem. Mater. *32*, 2430–2439.

Yu, D., Zhou, Y., Ma, C., Melman, J.H., Baroudi, K.M., LaCapra, M., and Riman, R.E. (2019). Non-rare-earth $Na_3AlF_6:Cr^{3+}$ phosphors for far-red light-emitting diodes. ACS Appl. Electron. Mater. *1*, 2325–2333.

Zhang, L., Wang, D., Hao, Z., Zhang, X., Pan, G.-h., Wu, H., and Zhang, J. (2019). Cr^{3+}-doped broadband NIR garnet phosphor with enhanced luminescence and its application in NIR spectroscopy. Adv. Opt. Mater. *7*, 1900185.

Zhao, F., Song, Z., Zhao, J., and Liu, Q. (2019). Double perovskite $Cs_2AgInCl_6:Cr^{3+}$: broadband and near-infrared luminescent materials. Inorg. Chem. Front. *6*, 3621–3628.

Zhao, M., Li, B., Wu, Y., He, H., Zhu, X., Zhang, H., Dou, C., Feng, L., Fan, Y., and Zhang, F. (2020). A tumor-microenvironment-responsive lanthanide-cyanine FRET sensor for NIR-II luminescence-lifetime in situ imaging of hepatocellular carcinoma. Adv. Mater. *32*, 2001172.

Zhou, Z., Yi, X., Xiong, P., Xu, X., Ma, Z., and Peng, M. (2020). Cr^{3+}-Free near-infrared persistent luminescence material $LiGaO_2:Fe^{3+}$: optical properties, afterglow mechanism and potential bioimaging. J. Mater. Chem. C *8*, 14100–14108.

iScience, Volume *24*

Supplemental information

Li/Na substitution and Yb^{3+} co-doping enabling tunable near-infrared emission in $LiIn_2SbO_6:Cr^{3+}$ phosphors for light-emitting diodes

Gaochao Liu, Tao Hu, Maxim S. Molokeev, and Zhiguo Xia

Supplemental Figures

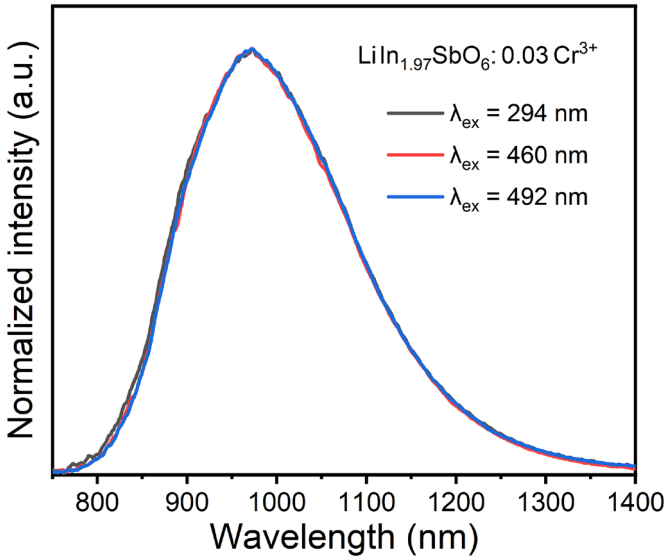

Figure S1. Normalized PL spectra of $LiIn_{1.97}SbO_6$:0.03Cr^{3+} under 294 nm, 460 nm and 492 nm excitation, related to Figure 2A.

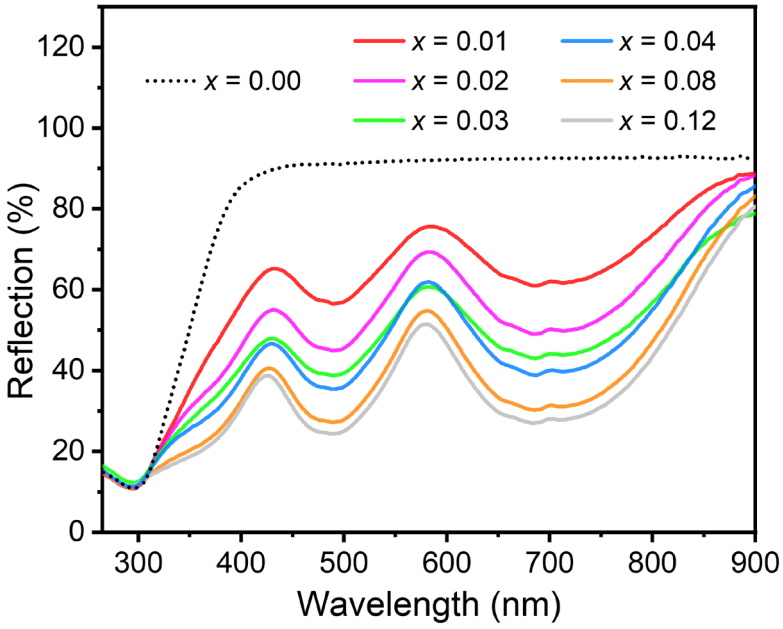

Figure S2. UV-VIS-NIR diffuse reflectance spectra of $LiIn_{2-x}SbO_6:xCr^{3+}$ (x = 0 - 0.12) phosphors, related to Figure 2B.

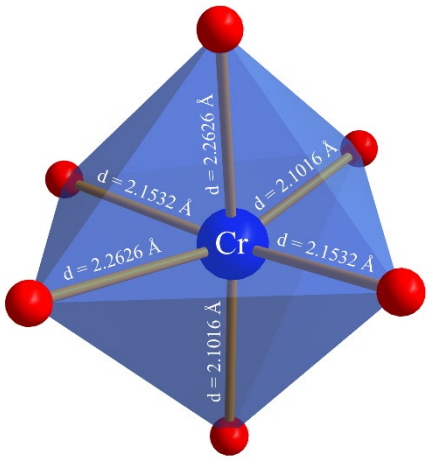

Figure S3. Distorted coordinate octahedron of Cr^{3+} in $LiIn_2SbO_6$ host, related to Figure 2D.

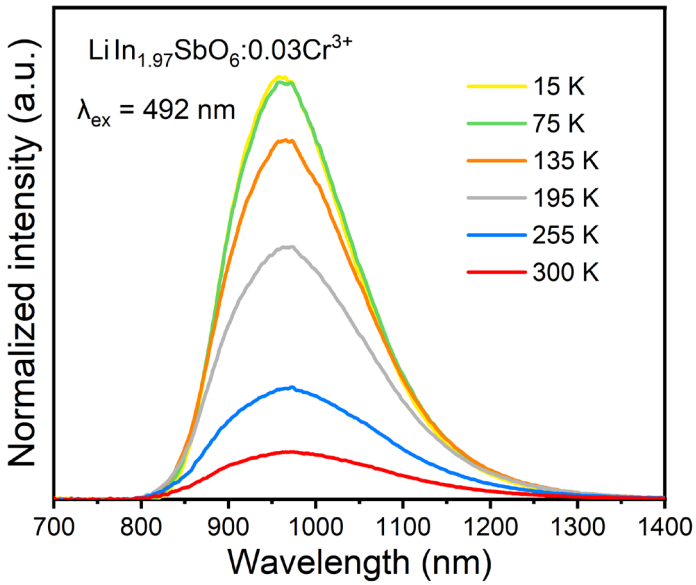

Figure S4. Temperature-dependent PL spectra of $LiIn_{1.97}SbO_6:0.03Cr^{3+}$ upon 492-nm excitation, related to Figure 3A.

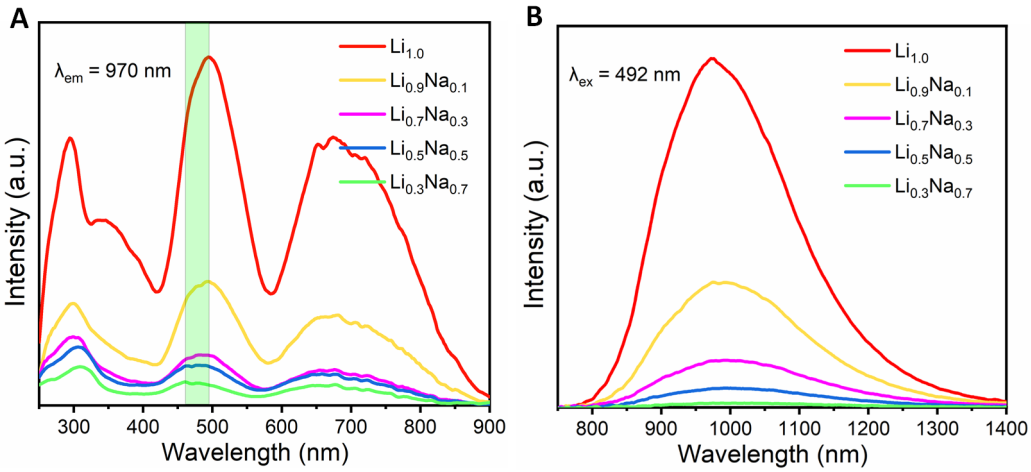

Figure S5. (A-B) Room-temperature PLE and PL Spectra of $(Li_{1-z}Na_z)In_{1.97}SbO_6$:0.03$Cr^{3+}$ (z = 0 - 0.7) phosphors, related to Figure 4C.

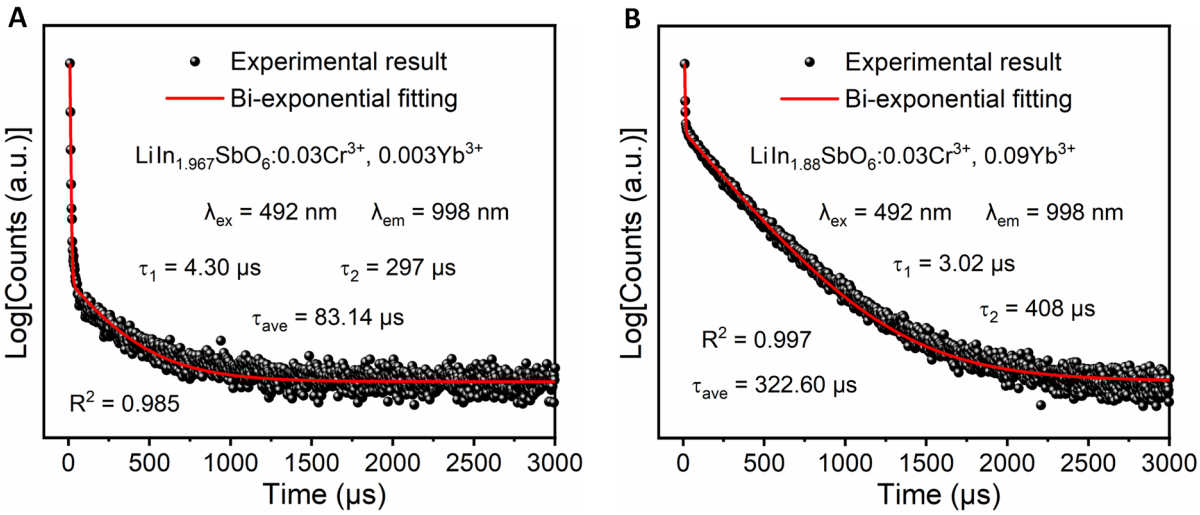

Figure S6. (A-B) Bi-exponential fitting of room-temperature fluorescence decay curve for $LiIn_{1.967}SbO_6$: $0.03Cr^{3+}$, $0.003Yb^{3+}$ and $LiIn_{1.88}SbO_6$:$0.03Cr^{3+}$, $0.09Yb^{3+}$, respectively, related to Figure 6B.

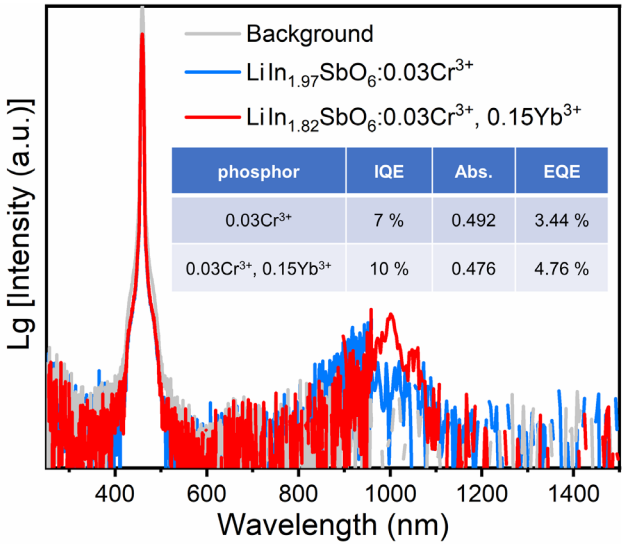

Figure S7. Integrated intensity of $LiIn_{1.97}SbO_6:0.03Cr^{3+}$ and $LiIn_{1.82}SbO_6:0.03Cr^{3+}$, $0.15Yb^{3+}$ for quantum yields measurements, related to Figure 8.

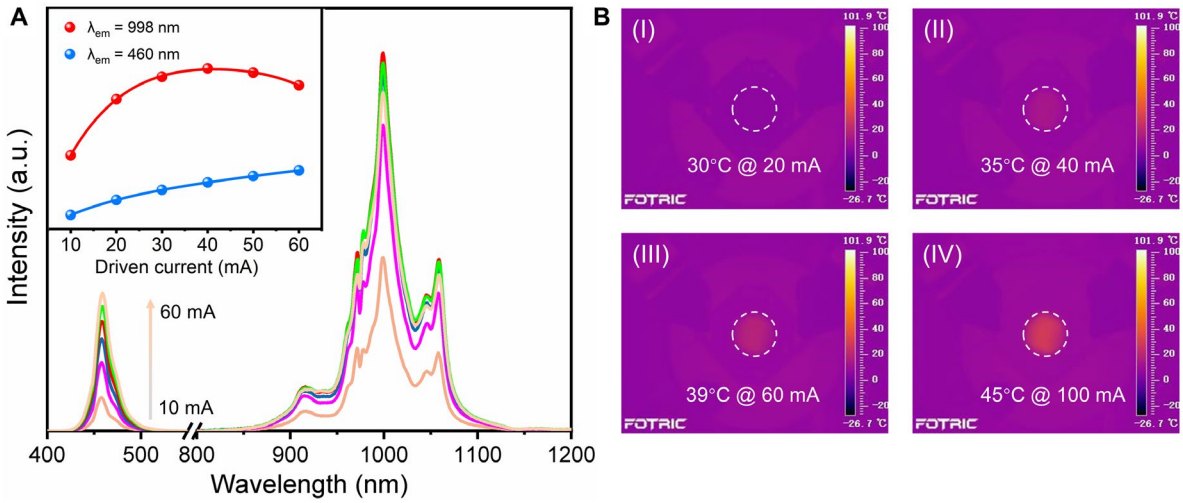

Figure S8. Luminous intensity and operating temperature of fabricated NIR pc-LED under variable current, related to Figure 8.

(A) Driven current dependent emission spectra of fabricated NIR pc-LED. The abnormal decrease at 973 nm may be caused by the absorption of curable adhesives.

(B) Thermographs at different driven currents from 20 mA to 100 mA.

Supplemental Tables

Table S1. Main refined structural parameters of the $LiIn_2SbO_6$:0.03Cr^{3+} sample, related to Figure 1.

Compound	$LiIn_2SbO_6$:0.03Cr^{3+}
Symmetry	Orthorhombic
Space group	*Pnnm*
a, Å	5.10471 (3)
b, Å	5.33298 (3)
c, Å	8.86988 (5)
V, $Å^3$	241.467 (2)
Z	2
2θ-interval, °	5-120
R_{wp}, %	6.66
R_p, %	5.08
R_B, %	1.05
χ^2	3.73

Table S2. Fractional atomic coordinates and isotropic displacement parameters (Å^2) of $LiIn_{1.97}SbO_6$:0.03Cr^{3+}, related to Figure 1.

Atom	*x*	*y*	*z*	B_{iso}	*Occ.*
Sb	0.5	0.5	0.5	0.7 (2)	1
In	0.5	0	0.30068 (8)	0.6 (2)	0.97
Cr	0.5	0	0.30068 (8)	0.6 (2)	0.03
Li	0.036 (16)	0.110 (6)	0.5	2.0 (12)	0.5
O1	0.2808 (16)	0.3343 (9)	0.3429 (9)	0.7 (3)	1
O2	0.698 (2)	0.1814 (16)	0.5	0.9 (3)	1

Table S3. Crystal field parameters of different Cr^{3+}-doped broadband NIR phosphors, related to Figure 2D and Figure S3.

Host	D_q (cm^{-1})	B (cm^{-1})	$\beta = B / B_0$	D_q / B	PL maximum	Reference
$Y_3Sc_2Ga_3O_{12}$	1587	635	0.69	2.50	740 nm	(Malysa, et al., 2018)
$Y_2CaAl_4SiO_{12}$	1647	678	0.74	2.43	744 nm	(Mao, et al., 2020)
La_2MgZrO_6	1589	628	0.68	2.53	825 nm	(Zeng, et al., 2019)
$Cs_2AgInCl_6$	1250	527	0.57	2.37	1010 nm	(Zhao, et al., 2019)
$Mg_4Ga_4Ge_3O_{16}$	1695	712	0.78	2.38	750 nm	(Zhan, et al., 2019)
$MgTa_2O_6$	1471	588	0.64	2.50	834 nm	(Liu, et al., 2020)
$LiIn_2SbO_6$	1428	616	0.67	2.32	970 nm	This work

Table S4. Spectroscopy and crystal field parameters of $Li_{1-z}Na_zIn_{1.97}SbO_6$:0.03$Cr^{3+}$ (z = 0 - 0.7) phosphors, related to Figure 4B.

Host	D_q (cm^{-1})	[$E(^4T_1)$-$E(^4T_2)$] (cm^{-1})	B (cm^{-1})	$\beta = B / B_0$	D_q / B
$Z = 0$	1428	6039.49	616.10	0.67	2.32
$Z = 0.1$	1435	6122.45	627.94	0.68	2.28
$Z = 0.3$	1432	6375.44	665.35	0.72	2.15
$Z = 0.5$	1436	6634.79	705.95	0.77	2.02
$Z = 0.7$	1440	7453.42	854.04	0.93	1.67

Transparent Methods

Synthesis of materials: Powder samples with compositions of $LiIn_{2-x}SbO_6$:xCr^{3+}, $Li_{1-z}Na_zIn_{1.97}SbO_6$:$0.03Cr^{3+}$ and $LiIn_{1.97-y}SbO_6$:$0.03Cr^{3+}$, yYb^{3+} ($0 \leqslant x \leqslant 0.12$, $0 \leqslant z \leqslant 0.9$ and $0 \leqslant y \leqslant 0.18$) phosphors were prepared through high temperature solid-state reaction method. The analytical reagents of $LiCO_3$ (99%, Aladdin), $NaCO_3$ (99.9%, Aladdin), In_2O_3 (99.9%, Aladdin), Sb_2O_3 (99.99%, Aladdin), Cr_2O_3 (99%, Aladdin) and Yb_2O_3 (99.99%, Aladdin) were used as raw materials. Typically, stoichiometric amounts of raw materials were weighted and put in an agate mortar. The mixtures were ground thoroughly for 15 minutes and then transferred into a corundum crucible and put into a muffle furnace to sinter at 1250℃ for 6 h in air. Finally, after the samples were naturally cooled down to room temperature, they were crushed to fine powders and stored in a chamber at the constant temperature and humidity for further measurements.

Sample characterization: The phase and purity of the as-prepared powder samples were examined by X-ray diffraction (XRD) analysis using a Bruker D8 ADVANCE power diffractometer with CuKα radiation source (λ = 0.15406 nm) and a linear VANTEC detector. The operation voltage and current were set as 40 kV and 15 mA, respectively. The data were collected in the range of 5°-120° with a step size of 0.0217 nm (2θ) and a count time of 5 s per step. Structural characterization and Rietveld refinement were conducted using *TOPAS 4.2* software. Room-temperature photo-luminescence (PL) spectra and PL excitation (PLE) spectra were recorded using a FLS920 fluorescence spectrophotometer equipped with a continuous xenon lamp (450 W) as an excitation source and a liquid-nitrogen cooled NIR photomultiplier tube as a detector (Hamamatsu, R5509, InP/InGaAsP). The PL decay curve was also measured by the same FLS920 instrument using a microsecond flash lamp (μF900) as the excitation source, and the statistical photons are 5000. The luminescence thermal quenching behavior of the samples was measured by the same spectrophotometer, which was equipped with a TAP-02 high- temperature fluorescence instrument (Tian Jin Orient - KOJI instrument Co., Ltd.). Photographs for the application of NIR pc-LEDs were taken by an industrial night-vision camera (MV-CA050-20GN, HIKVISION, China). The diffuse reflection (DR) spectra of the samples were recorded using an UV-Vis-NIR spectrophotometer (Hitachi High-Tech Science Corporation, UH4150) with $BaSO_4$ as a standard. The quantum efficiency at room temperature was measured by an absolute PL quantum yield spectrometer (Quantaurus - QY Plus C13534-12, Hamamatsu Photonics).

LEDs fabrication: The NIR LED was fabricated based on the as-synthesized NIR emitting phosphor and the chip-on-board (COB) blue LED (X1901, 5 W, Guangzhou LEDteen Optoelectronics Co., Ltd., China), and the mass ratio of the epoxy resin to NIR phosphor is fixed at 1:1. The blue InGaN chips in the COB LEDs are (S-35EBMUD-A, 450-452.5 nm, 2.9-3.1V/150 mA, San'an Optoelectronics co., LTD., China). The demonstration images were collected by an industrial night-vision camera (MV-CA050-20GN, HIKVISION, China). Meanwhile, the temperatures of the fabricated working NIR LEDs were recorded by a thermal infrared camera (Fotric 225S).

Supplemental References

B. Malysa, A. Meijerink and T. Jüstel. (2018). Temperature dependent Cr^{3+} photoluminescence in garnets of the type $X_3Sc_2Ga_3O_{12}$ (X = Lu, Y, Gd, La). J. Lumin. *202*, 523-531.

M. Mao, T. Zhou, H. Zeng, L. Wang, F. Huang, X. Tang and R.-J. Xie. (2020). Broadband near-infrared (NIR) emission realized by the crystal-field engineering of $Y_{3-x}Ca_xAl_{5-x}Si_xO_{12}:Cr^{3+}$ (x = 0-2.0) garnet phosphors. J. Mater. Chem. C. *8*, 1981-1988.

H. Zeng, T. Zhou, L. Wang and R.-J. Xie. (2019). Two-Site occupation for exploring ultra-broadband near-infrared phosphor—double-perovskite $La_2MgZrO_6:Cr^{3+}$. Chem. Mater. *31*, 5245-5253.

F. Zhao, Z. Song, J. Zhao and Q. Liu. (2019). Double perovskite $Cs_2AgInCl_6:Cr^{3+}$: broadband and near-infrared luminescent materials. Inorg. Chem. Front. *6*, 3621-3628.

Y. Zhan, Y. Jin, H. Wu, L. Yuan, G. Ju, Y. Lv and Y. Hu. (2019). Cr^{3+}-doped $Mg_4Ga_4Ge_3O_{16}$ near-infrared phosphor membrane for optical information storage and recording. J. Alloys Compd. *777*, 991-1000.

G. Liu, M. S. Molokeev, B. Lei and Z. Xia. (2020). Two-site Cr^{3+} occupation in the $MgTa_2O_6:Cr^{3+}$ phosphor toward broad-band near-infrared emission for vessel visualization. J. Mater. Chem. C. *8*, 9322-9328.